

A high resolution gamma-ray spectrometer based on superconducting microcalorimeters

D. A. Bennett, R. D. Horansky, D. R. Schmidt, A. S. Hoover, R. Winkler, B. K. Alpert, J. A. Beall, W. B. Doriese, J. W. Fowler, C. P. Fitzgerald, G. C. Hilton, K. D. Irwin, V. Kotsubo, J. A. B. Mates, G. C. O'Neil, M. W. Rabin, C. D. Reintsema, F. J. Schima, D. S. Swetz, L. R. Vale, and J. N. Ullom

Citation: [Review of Scientific Instruments](#) **83**, 093113 (2012); doi: 10.1063/1.4754630

View online: <http://dx.doi.org/10.1063/1.4754630>

View Table of Contents: <http://scitation.aip.org/content/aip/journal/rsi/83/9?ver=pdfcov>

Published by the [AIP Publishing](#)

Articles you may be interested in

[High-resolution gamma-ray spectroscopy with a microwave-multiplexed transition-edge sensor array](#)
Appl. Phys. Lett. **103**, 202602 (2013); 10.1063/1.4829156

[14 - pixel , multiplexed array of gamma-ray microcalorimeters with 47 eV energy resolution at 103 keV](#)
Appl. Phys. Lett. **90**, 193508 (2007); 10.1063/1.2738371

[Time-division multiplexing of high-resolution x-ray microcalorimeters: Four pixels and beyond](#)
Appl. Phys. Lett. **85**, 4762 (2004); 10.1063/1.1823041

[Magnetic calorimeters for high resolution x-ray spectroscopy](#)
Rev. Sci. Instrum. **74**, 3947 (2003); 10.1063/1.1597952

[SQUID-based readout schemes for microcalorimeter arrays](#)
AIP Conf. Proc. **605**, 295 (2002); 10.1063/1.1457649

Nor-Cal Products



Manufacturers of High Vacuum
Components Since 1962

- Chambers
- Viewports
- Valves
- Motion Transfer
- Foreline Traps
- Flanges & Fittings
- Feedthroughs



www.n-c.com
800-824-4166

A high resolution gamma-ray spectrometer based on superconducting microcalorimeters

D. A. Bennett,^{1,2} R. D. Horansky,^{1,2} D. R. Schmidt,^{1,3} A. S. Hoover,⁴ R. Winkler,⁴
B. K. Alpert,¹ J. A. Beall,¹ W. B. Doriese,^{1,3} J. W. Fowler,^{1,3} C. P. Fitzgerald,¹ G. C. Hilton,¹
K. D. Irwin,¹ V. Kotsubo,^{1,3} J. A. B. Mates,^{1,3} G. C. O'Neil,¹ M. W. Rabin,⁴ C. D. Reintsema,¹
F. J. Schima,¹ D. S. Swetz,¹ L. R. Vale,¹ and J. N. Ullom¹

¹National Institute of Standards and Technology, Boulder, Colorado 80305, USA

²University of Denver, Denver, Colorado 80208, USA

³University of Colorado, Boulder, Colorado 80309, USA

⁴Los Alamos National Laboratory, Los Alamos, New Mexico 87545, USA

(Received 17 July 2012; accepted 9 September 2012; published online 28 September 2012)

Improvements in superconductor device fabrication, detector hybridization techniques, and superconducting quantum interference device readout have made square-centimeter-sized arrays of gamma-ray microcalorimeters, based on transition-edge sensors (TESs), possible. At these collecting areas, gamma microcalorimeters can utilize their unprecedented energy resolution to perform spectroscopy in a number of applications that are limited by closely-spaced spectral peaks, for example, the non-destructive analysis of nuclear materials. We have built a 256 pixel spectrometer with an average full-width-at-half-maximum energy resolution of 53 eV at 97 keV, a useable dynamic range above 400 keV, and a collecting area of 5 cm². We have demonstrated multiplexed readout of the full 256 pixel array with 236 of the pixels (91%) giving spectroscopic data. This is the largest multiplexed array of TES microcalorimeters to date. This paper will review the spectrometer, highlighting the instrument design, detector fabrication, readout, operation of the instrument, and data processing. Further, we describe the characterization and performance of the newest 256 pixel array.

© 2012 American Institute of Physics. [<http://dx.doi.org/10.1063/1.4754630>]

I. INTRODUCTION

Gamma-ray microcalorimeters based on transition-edge sensors (TES) have demonstrated FWHM energy resolutions of 22 eV at 97.4 keV,¹ more than an order of magnitude better than state-of-the-art high-purity germanium detectors (HPGe). Recent developments in the modeling and fabrication of TESs, along with advances in multiplexing, have allowed microcalorimeter arrays to approach efficiencies typical for HPGe detectors. The TES microcalorimeter's combination of energy resolution and efficiency has the potential to benefit a number of measurement scenarios that require the ability to resolve closely spaced spectral peaks and to reveal previously indistinguishable spectral features.²

A TES consists of a thin superconducting film that is voltage-biased in the transition between the superconducting and normal states.³ In the transition, a small change in the temperature of the TES results in a large change in the resistance of the device so that the TES acts as a very sensitive thermometer. The TES is operated as a photon detector by thermally linking the TES to some object that converts the energy of an incoming photon to heat. The heating of the TES causes the resistance of the film to increase and the bias current flowing through the device to decrease. Microcalorimeters achieve high energy resolution by operating at low temperatures (≈ 100 mK) with small heat capacities.

The instrument described in this paper is intended to enable more accurate measurement of the quantities of isotopes in nuclear samples from high-statistics spectra that re-

solve isotope-specific gamma-ray lines.⁴ Improved resolving power is useful in a number of measurement scenarios that benefit from rapid nondestructive analysis of complicated mixed-isotope samples. These measurement scenarios arise in nuclear safeguards where the ability to detect material diversion is directly linked to measurement precision and accuracy.

The energy resolution for HPGe detectors is fundamentally limited by fluctuation in the number of charge carriers created when a photon is absorbed. This fundamental limit gives a FWHM energy resolution of 400 eV at 122 keV. In practice, these limits are approached only by smaller planar germanium detectors, and the achieved energy resolution is usually higher. As will be shown in Sec. II, the energy resolution that can be obtained by use of microcalorimeters is more than an order of magnitude, better than what is possible with semiconducting detectors.

Figure 1 demonstrates the microcalorimeter's ability to resolve closely spaced lines in Pu samples. It shows a spectrum of a reference sample that contains roughly 0.4 g of Pu (85% ²³⁹Pu and 14% ²⁴⁰Pu) measured by use of both a HPGe detector (red) and an earlier 64-pixel array of microcalorimeters (black).¹⁰ The plot focuses on a congested region of the spectrum between 96 and 105 keV. The microcalorimeters are able to resolve the ²³⁹Pu peak at 98.78 keV despite the presence of the ²⁴¹Am peak at 98.97 keV and the U K α_1 peak at 98.43 keV.

Pu spectra with sufficient statistics to determine relative isotope mass to 0.5% require tens of millions of counts. In order to measure such a spectrum in reasonable times,

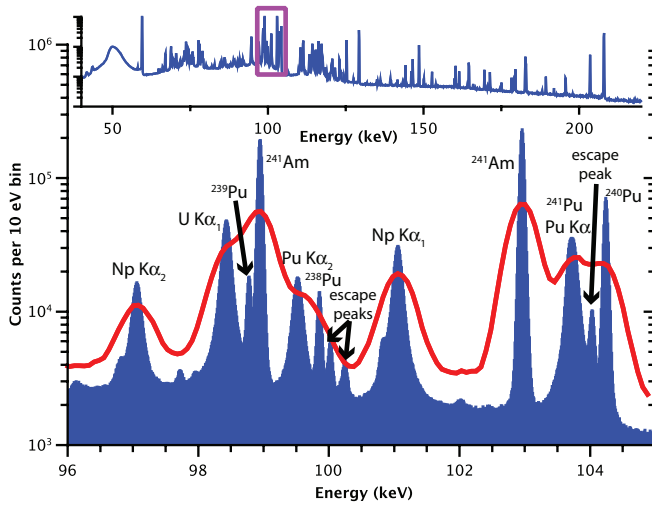


FIG. 1. A measured spectrum of roughly 0.4 g of Pu (85% ^{239}Pu and 14% ^{240}Pu) comparing results with an array of microcalorimeters (blue) and a high-purity germanium detector (red). The inset shows the same spectrum over the energy range 40 keV to 220 keV.

system count rates of at least a kilohertz are required. For faint sources, large collecting areas are also important.

Much of the literature about microcalorimeters for gamma-ray spectroscopy has focused on the detectors themselves or analysis of spectra as opposed to the design and operation of an entire instrument. This paper will address the NIST-LANL gamma-ray spectrometer at an instrument level including details of the experimental setup, fabrication of the detectors, readout, operation of the instrument, and data processing. We will also describe the characterization and performance of the instrument.

II. TES MICROCALORIMETER THEORY

Transition-edge sensors have been used to detect photons and particles over a wide energy range that spans sub-millimeter photons and MeV alpha particles. Although TES microcalorimeters can be used over the whole range of x-ray and gamma-ray energies, the best performance is obtained when the device parameters are optimized for the individual application. In this section, we describe the optimization of our TES microcalorimeter spectrometer. We briefly discuss the important considerations in instrument design, including tradeoffs in energy resolution, dynamic range, speed, and efficiency.

Figure 2(a) shows a schematic representation of the coupled electrical and thermal circuits of a TES microcalorimeter with a thermally linked bulk absorber. The TES is separated from the thermal bath by a weak thermal conductance (G_1). When current is flowing through the resistance (R_0) of the TES, its heat capacity (C_1) is heated to a temperature (T_1) above the bath temperature (T_b) by the electrical bias. The sensor is voltage biased by placing its resistance (R_0) in parallel with the smaller shunt resistance (R_{sh}). The equilibrium current in the TES (I_0) can then be chosen so that the equilibrium temperature (T_0) is in the superconducting transition yielding a value of R_0 that is in-between the normal resistance

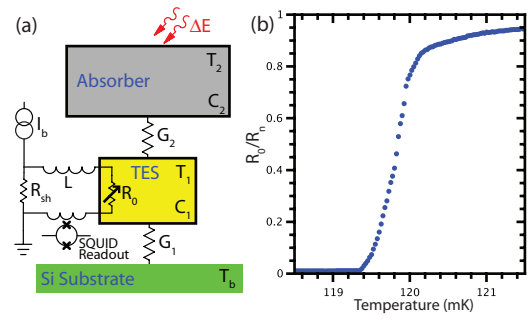


FIG. 2. (a) Schematic representation of the coupled electrical and thermal circuits of a two-body TES. The thermal conductances are shown as resistors. (b) A typical superconducting transition for a Mo-Cu TES at zero dc current with a small ac current used to perform the measurement.

(R_n) and zero resistance, see Fig. 2(b). In the small-signal limit, the transition is parameterized by use of the logarithmic temperature sensitivity at constant current

$$\alpha_I = \left. \frac{\delta \log R}{\delta \log T} \right|_{I_0} = \left. \frac{T_0}{R_0} \frac{\delta R}{\delta T} \right|_{I_0}, \quad (1)$$

and the logarithmic current sensitivity at constant temperature

$$\beta_I = \left. \frac{\delta \log R}{\delta \log I} \right|_{T_0} = \left. \frac{I_0}{R_0} \frac{\delta R}{\delta I} \right|_{T_0}, \quad (2)$$

so that the TES resistance as a function of changes in temperature and current is Taylor expanded with only first order terms retained

$$R_{TES}(\delta T, \delta I) \approx R_0 + \alpha_I \frac{R_0}{T_0} \delta T + \beta_I \frac{R_0}{I_0} \delta I. \quad (3)$$

For simplicity, we start by assuming the thermal conductance between the absorber and TES (G_2) is large, so that heat capacity of the absorber (C_2) and C_1 act as a single heat capacity given by $C = C_1 + C_2$. When a photon strikes C , the temperature of the TES and the absorber rises momentarily, but then returns to equilibrium as the additional energy flows through G_1 into the bath. If we decouple the electrical and thermal portions of the circuit, an instantaneous increase in resistance would cause an exponential drop in current with a time constant $\tau_{el} = L/(R_{sh} + R_0)$. The inductance (L) has the effect of slowing down the current change. Then the temperature of the TES returns to equilibrium exponentially with a time constant $\tau = C/G_1$. The current through the TES is the sum of the exponential decrease in current limited by τ_{el} (rise time of pulse) and an exponential return to equilibrium (fall time of pulse) given by τ .

When the electrical and thermal circuits of the TES are coupled, the decay time back to thermal equilibrium is reduced by negative electro-thermal feedback (ETF).³ When the temperature of the film is increased by a photon or thermal fluctuations, the resistance goes up, then the current drops, causing the Joule heating to go down, driving the temperature back to the equilibrium value. As with most feedback mechanisms, the ETF can cause the TES to become unstable when the feedback overcompensates. Care must be taken in choosing the TES parameters to ensure stable detectors.

Stability is evaluated by solving the linearized differential equations that describe the full coupled electrical and thermal circuits.³

The voltage-biased TES converts the energy of the incident photon into a current pulse. This current is inductively coupled to a DC superconducting quantum interference device (SQUID), which is well matched to the low impedance of a voltage-biased TES. As will be discussed later in Sec. IV C, the SQUID is also an ideal amplifier because it is compatible with a number of schemes for large-scale multiplexed readout.

Finally, a bulk absorber is added to stop energetic photons in the 20 keV range and above. In the energy range of this instrument, the absorption of an x-ray or gamma-ray in a bulk superconductor occurs primarily by photoelectric absorption that creates an energetic photoelectron. The electron down-converts through a series of electron-electron and electron-phonon interactions. The end product is a population of phonons that escape into the TES. The method of attachment determines the thermal conductance G_2 between the absorber and the TES. The explicit two-body nature of these gamma-ray devices necessitates moving beyond the simple, one-body thermo-electric model for design and optimization.⁵

Since improved energy resolution is one motivating factor behind this instrument, it is useful to examine the parameters that determine the energy resolution. The heat capacity of the absorber determines how much of a temperature change occurs for deposited photon energy. When the electrothermal feedback is strong and β_I is small, the change of resistance with a change in temperature is determined mostly by α_I . In this limit, the energy resolution³ scales as $\Delta E \propto \sqrt{T_c^2 C / \alpha_I}$.

We must further consider the dynamic range of the instrument, which depends on T_c , C , and α_I . We define the saturation energy (E_{sat}) as the photon energy that would cause the TES to increase temperature to the point where the resistance equals R_n . At this energy, the current pulses have flat tops, causing degraded energy resolution. We can roughly approximate the saturation energy⁶ as $E_{sat} \approx 4T_c C / \alpha_I$, where we have assumed that the transition is linear and that the device is biased at 20% of R_n . A decrease in C or an increase in α_I improves the energy resolution but at the cost of reduced dynamic range. Therefore, optimizing instrument performance requires carefully selecting C and α_I .

III. TES GAMMA-RAY MICROCALORIMETER

The design goals of this instrument are to measure gamma-ray spectra with the best resolution possible for energies from 20 keV to 220 keV, while achieving efficiencies and count rates similar to those of HPGe detectors. Section II described the operation of a TES and how it can be optimized for very-high-resolution measurements. This section describes practical considerations that affect the TES spectrometer, including micro-fabrication, operating temperatures, and multiplexed readout, and how these are balanced with energy resolution and efficiency.

A. Instrument constraints and pixel design

Impressive energy resolution has been achieved by use of TES microcalorimeters (22 eV at 97.4 keV), by using small heat capacities (3 pJ/K) and low temperatures (94 mK).^{1,7} To achieve this low heat capacity, a tin absorber that was 900 μm on a side by 220 μm thick was used as the photon absorber. For a single microcalorimeter, this provides a 26% chance of absorbing an incident 100 keV photon within the area of the absorber and a 2.68×10^{-7} total efficiency for a point source 25 cm away. It would take unreasonable time to obtain enough counts to obtain high statistics spectra capable of determining isotopic composition in relevant samples. The need for improved efficiency drives the instrument design towards larger absorbers to improve the per-pixel efficiency, and arrays of microcalorimeters to improve the absolute efficiency.

Use of arrays of TES microcalorimeters improves the collecting area and thus the efficiency, but potentially requires a SQUID to read out each detector. Between the wires needed for detector bias and readout, the total wire count can quickly climb to numbers where the thermal load makes the cryogenics difficult and expensive. For this reason, arrays are usually read out using one of several multiplexing techniques.³ In these techniques, multiple detectors are grouped together in columns that share much of the readout chain to reduce wire count. The instrument described here uses time-division multiplexing (TDM). TDM has previously demonstrated multiplexed readout of a 10 240 pixel array of bolometers.⁸ Multiplexing microcalorimeters is more difficult since the current changes much faster than in a bolometer. When using TDM to multiplex microcalorimeters, the bandwidth required grows as the number of detectors in a column gets larger and as the rate of change of signal from the detectors increases. As will be described in Sec. IV C, we calculate that we should be able to multiplex 32 rows in each column. As will be described in Sec. IV E, we need approximately 256 pixels to achieve the desired efficiency, setting the array format to be 8 columns by 32 rows.

A compelling choice for the T_c of the TES is in the region between 100 mK and 150 mK. These T_c s provide suitable energy resolution and allow the use of adiabatic demagnetization refrigerators, a relatively inexpensive and robust cryogenic refrigerator. The T_c can be tuned over a broad range of temperatures by taking advantage of the proximity effect in thin-film bilayers, where one layer is a superconductor with T_c above the temperature of interest, such as molybdenum ($T_c = 0.92$ K), and the other layer is a normal metal, such as copper or gold. The Mo-Co bilayer, shown in the middle of Fig. 3(a), is 400 μm by 400 μm and has a $T_c = 120$ mK. Eight Cu bars are added to the Mo-Cu film to control the transition width⁶ and reduce noise.⁹

The low thermal conductance from the Mo-Cu TES to the Si substrate is achieved by placing the TES on a Si_3N_4 membrane that is 1 μm thick. The Si_3N_4 membrane is 1.4 mm by 1.4 mm and is the darker area that takes up most of the picture in Fig. 3(a). The thickness and size of the Si_3N_4 are chosen to match the footprint of the absorber and achieve a target G_1 of approximately 3 nW/K. The bulk absorber is attached by glue to 20 epoxy posts distributed around the membrane

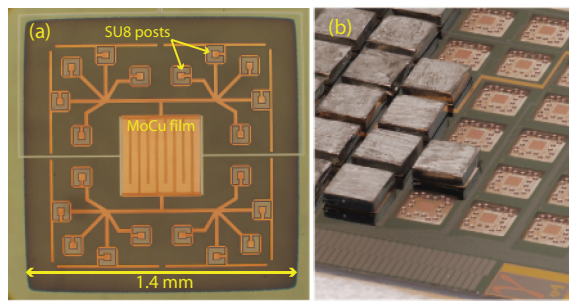


FIG. 3. (a) Photograph of a TES microcalorimeter before the absorber is attached showing the Si_3N_4 membrane (darker area), TES in the middle, and 20 SU8 posts connected to the TES by the copper legs. (b) A portion of one of the detector chips where some of the TES have been absorberized.

(Fig. 3(a)). The posts are connected to the Mo-Cu film by copper traces of equal length to ensure that heat traveling through any one of the posts has a similar thermal path to the Mo-Cu film.

The absorbers, shown for a few of the pixels in Fig. 3(b), are 1.45 by 1.45 mm by 0.38 mm thick pieces of polycrystalline Sn. Sn is chosen because it has reasonably high efficiency for stopping gamma rays in the energy range of interest (20 keV to 220 keV), while still having low specific heat near 120 mK. The transition temperature of Sn is 3.7 K, well above the operating temperature of these devices. In this case, the phonon contribution, which scales as T^3 , dominates over the electron contribution to the specific heat, which scales as $e^{-\Delta/k_B T}$. The heat capacity of the tin absorber is predicted to be 22.5 pJ/K, using the Debye temperature of bulk tin, 195 K, and a device temperature near $T_c = 120$ mK. We can estimate the energy resolution of these devices by scaling the 22 eV FWHM energy resolution result from Bacrania *et al.*¹ up to the design values of C and T_c to predict a FWHM energy resolution of 77 eV. On a previous array¹⁰ with Sn absorbers 2.25 mm² by 0.25 mm thick, we achieved energy resolutions consistent with this scaling.

B. TES array fabrication and detector hybridization

Large arrays of TES sensors are made possible by modern microfabrication techniques. The detector fabrication process starts with 3 in. Si wafers. The wafers are 275 μm thick and polished on both sides. We grow 120 nm of SiO_2 on the wafers by use of wet thermal oxidation. Then we deposit 1 μm of stoichiometric silicon-nitride (Si_3N_4) by use of low pressure chemical vapor deposition. We etch alignment marks into the Si_3N_4 on the front side of the wafers.

We then deposit a superconducting bilayer of Mo and Cu with dc-magnetron sputtering. The Mo and Cu thicknesses are chosen to give suitable device T_c and R_N . Typically, the Mo is 100 nm thick and the Cu 200 nm. Using two lithography and wet etch steps, we pattern the bilayer into TESs with Mo leads. A wide border of bilayer is left around the perimeter of each die. In the next step, we use lift-off lithography and electron-beam evaporation to deposit the Cu banks on the edge of the TESs and bars, which extend from the banks onto the TES bilayer. The thickness of this additional Cu layer is

500 nm. We designed the pattern for this step to also place Cu around the perimeter of the chip to aid heat-sinking. A subsequent lift-off step is used to place 100 nm of Au on the perimeter to facilitate heat-sink wire-bonding. The last step on the front side is to form the posts for absorber hybridization. We first deposit 15 nm of Ti using lift-off in the post locations to aid post adhesion. We then use SU8, a photo-imageable epoxy, to form posts that are 35 μm tall.

We conduct the final processing steps on the backside of the wafer. We affix the frontside of the wafer to a similarly sized sapphire carrier wafer using wax. The Si_3N_4 and SiO_2 are stripped from the backside by use of reactive ion etching. We deposit a 1 μm Au backside thermal heat sink layer by use of a lift-off process. Then we use a Bosch-process Si deep etch to remove the Si behind each TES to form Si_3N_4 membranes. The deep-etch step also separates the wafer into dies. We extract the individual die by thermally reflowing the wax layer and sliding the die off the sapphire carrier wafer. The die is then solvent-cleaned to remove the wax.

Absorber attachment begins with preparation of the Sn. The 99.99+ percent pure Sn is crushed in a vise to the desired thickness of 0.38 mm. The cold working of the Sn increases its hardness, allowing cleaner cuts with a dicing saw. Previous experiments have shown that the change in grain size from this cold working does not affect the performance of Sn as a gamma-ray absorber in microcalorimeters.¹¹ We then dice the Sn into 1.45 mm squares with a diamond blade.

Each Sn absorber is physically attached by glue to 20 posts made of a photo-imagable epoxy (SU8) by use of a die bonder. The bonder has a micromanipulator with an 8:1 ratio and contains both a tweezer used to hold the glue applicator and a vacuum tool to pick up the absorber. A controlled amount of glue is applied to all of the posts of a single detector and then the absorber is placed on the posts and left to dry. The die bonder also allows the same force to be applied to each absorber. This process consistently yields well over 90% attachment. For a small number of microcalorimeters per chip, the glue used to attach the absorber can spread too far and cause a thermal short to the silicon wafer. We are making design changes and process improvements to eliminate these glue shorts and achieve close to 100% attachment yield.

IV. INSTRUMENT DESIGN AND EXPERIMENTAL SETUP

A. Cryogenics

The key advantage of superconducting microcalorimeters is derived from low-temperature operation, because energy resolution scales as $\Delta E \propto T_c$. The NIST-LANL gamma spectrometer achieves low temperatures by use of a pulse-tube-backed adiabatic demagnetization refrigeration (ADR) capable of cooling the detector package to a base temperature of 50 mK without the use of liquid cryogenics. The absence of liquid cryogenics allows convenient use of the instrument by non-experts outside of specialized cryogenic laboratories.

The cryostat is shown in Fig. 4 along with the detector housing. The left side of Fig. 4 shows a schematic

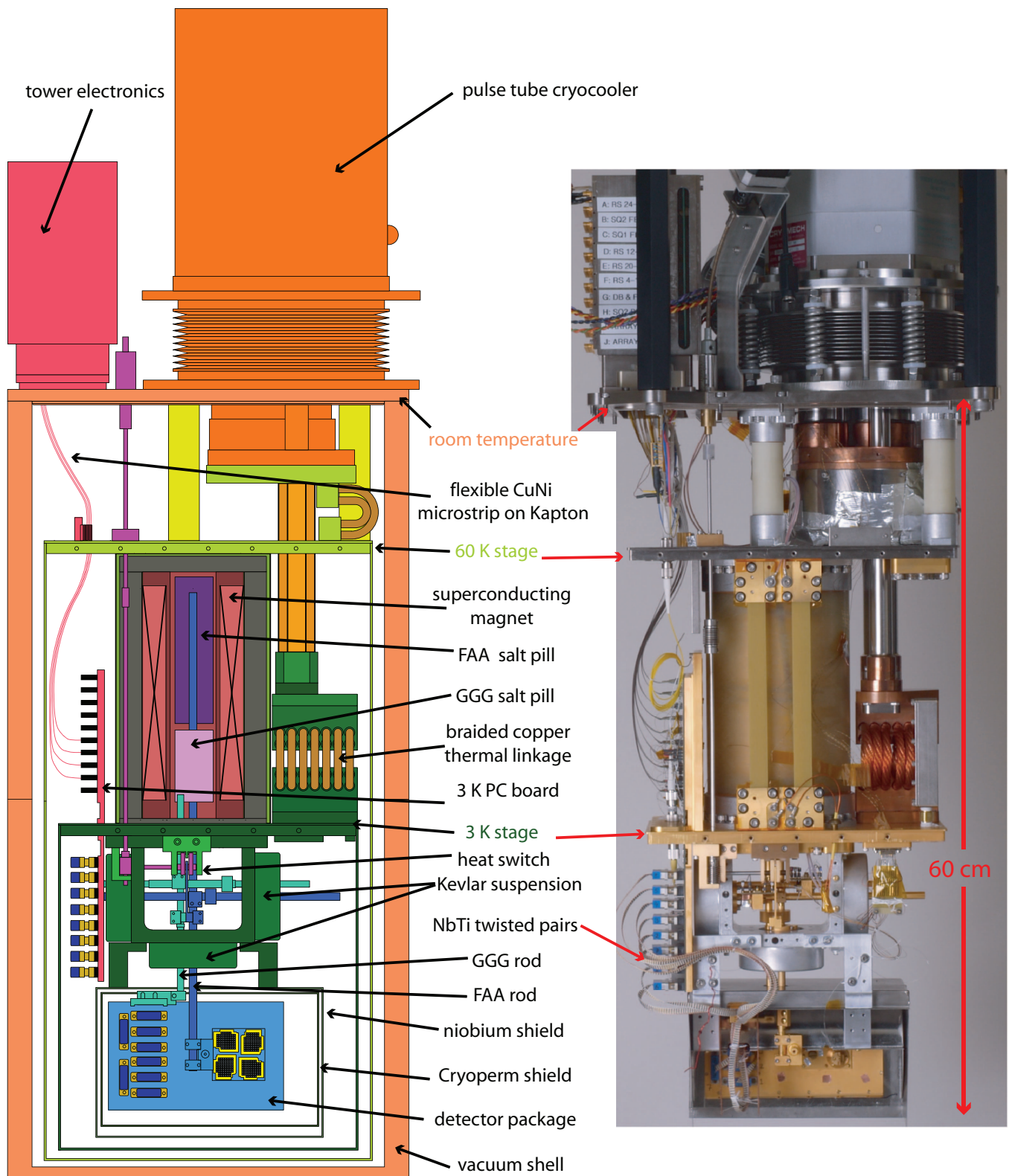


FIG. 4. A schematic view (left) and a photograph (right) of the NIST-LANL gamma spectrometer with the vacuum jacket and radiation shields removed.

representation of the apparatus noting the various temperature stages. With the vacuum jacket attached, the cryostat is 33 cm by 22 cm by 66 cm tall and has a mass of approximately 70 kg. With the wiring and detectors installed, the first-stage base temperature is around 60 K, while the second-stage temperature is usually around 3.5 K. The pulse-tube cooler uses

a two-stage configuration with a nominal cooling power of 25 W at 55 K in the first stage and 0.7 W at 4 K for the second stage. The pulse-tube heads are connected to the cryostat by flexible copper braid to conduct heat while reducing vibrations from the pulse tube. The spinning valve for the pulse-tube is mounted remotely on a separate stand and connected

to the pulse tube head by a flexible hose to also reduce vibrations. Wiring from room temperature is heat sunk both at the 60 K stage and the 3.5 K stage. There are also nested radiation shields at both stages.

An adiabatic demagnetization refrigerator utilizes the strong magnetocaloric effect in certain materials to cool the experimental stage of a cryostat. The magnetocaloric effect describes the heating or cooling of a material in a magnetic field due to coupling between the magnetic spins in the material and an applied magnetic field.¹² A paramagnetic material that acts as the refrigerant is thermally isolated from the 3 K stage of the cryostat and thermally connected to the objects to be cooled. A heat switch, shown in Fig. 4, allows ADR stages to be connected and disconnected to the higher temperature stages, as needed.

The ADR used for this instrument is a two-stage design with both gadolinium-gallium garnet (GGG) and ferric ammonium alum (FAA) pills, see Fig. 4. The GGG pill has a higher base temperature, nominally 600 mK to 700 mK in this setup, and higher heat capacity. The FAA pill can achieve lower temperature, nominally 40–50 mK, but has less heat capacity. Kevlar string tensioned around supporting posts in a star pattern is used to suspend the support rods of the GGG stage and FAA stage in series so that the GGG stage intercepts heat flow from 3K to the FAA stage. The heat load on the FAA stage is further reduced by heat-sinking the detector array wiring (approximately 200 superconducting wires) at the GGG temperature stage. The magnet is a NbTi superconducting magnet with a rated magnetic field of 4 T at 9 A and an inductance of 30 H.

The instrument typically achieves a base temperature of 40 mK with a standard magnet cycle, and a hold time of 25 h at 85 mK with the array wiring in place. During operation, with the array and readout biased, the hold time is 21 h for a two hour recycle time. This hold time is sufficient to obtain a high-statistic measurement in a single ADR cycle.

B. Magnetic shielding

As in most superconducting devices, the microcalorimeters and the SQUID readout are sensitive to magnetic fields. For a TES, the T_c , width of the superconducting transition, and amount of excess noise are dependent on magnetic fields.¹³ Furthermore, the heat capacity of the superconducting absorbers can be affected by a trapped magnetic field that keeps portions of the absorber normal. In order to mitigate the effects of magnetic fields, we have designed various levels of shielding into the cryostat.

The ADR magnet is surrounded by a vanadium permendur shield, an alloy of iron, cobalt, and vanadium with a high saturation induction (2.4 T). The vanadium permendur shields the sensors by reducing the fringing field of the magnet. At the peak 4 T field in the bore of the magnet, the external field is below 2 mT outside the cryostat at a radial distance of 122 mm from the center of the magnet bore. A thicker shield could attenuate more of the field but at the cost of adding significant thermal mass. During standard temperature regulation, the magnet's field is on the order of 50 mT. At 122 mm from

the center of the bore, the external field is reduced to 20 μ T. Based on these measurements we calculate a 2 μ T field in the vicinity of the detector box located 30 cm below and 4 cm radially from the center of the magnet. These fields are similar to those produced by the remnant magnetization of the vanadium permendur (30 μ T at 122 mm from the bore) and the background magnetic field in the laboratory.

The detector package is shielded from the superconducting magnet and stray magnetic fields in the laboratory by both superconducting niobium and high permeability shields. The Nb superconducting shield provides good protection from changing magnetic fields, but is susceptible to trapping flux as it goes through its transition temperature. The high-permeability shield is designed to have its highest permeability at cryogenic temperatures and provides a factor of 10^3 of field attenuation. The average measured magnetic field required to null the field inside all of the shielding at the detector box was 0.8 μ T. Finally, when the Sn absorbers directly on top of the TESs go superconducting, they provide additional shielding. As long as the magnetic field is reduced enough not to trap flux in the Sn absorbers, no field dependence is observed in the TESs.

C. TES readout

If a dedicated amplifier chain were used for each TES, heating would be a significant problem, due both to the thermal conductance of the wires and power dissipation. Multiplexing is necessary to reduce the heating caused by scaling to 256 pixels and will be critical to the success of even larger arrays. The advantages and disadvantages of different multiplexing schemes for TESs are described in detail elsewhere.³ SQUIDs are the ideal first stage amplifiers for TESs since they are low noise, low impedance, and low power devices. This instrument uses time-division multiplexing (TDM) that has successfully demonstrated the necessary speed and noise levels to read out gamma-ray TESs without significant degradation of energy resolution.⁷ General details of the NIST TDM multiplexing system are described by Reintsema *et al.*¹⁴ In this section, we will discuss the details of TDM multiplexing necessary to illustrate the tradeoffs made in this instrument.

Each TES is coupled to a first-stage SQUID (SQ1) in an 8-column by 32-row format. The signals from all the SQUIDs in a column are summed into a single second-stage SQUID (SQ2). Due to the intrinsic nonlinearity of the SQUID response, a digital flux-lock loop (FLL) is used to provide feedback to SQ1 and keep it operating where the SQUID error signal is always linearly proportional to the changes of flux being applied. The feedback coils for all of the SQ1s in a column are connected in series by use of a single wire. Each SQ1 in the column is biased sequentially so that only one row in each column is on at any given time. The SQ1 biases for a row are connected in series to bias that row in all 8 columns with a single wire. The SQ2 in each column requires a voltage bias and a flux bias. The signal from each SQ2 is then amplified by a SQUID series array¹⁵ mounted at 3.5 K and then amplified again at the top of the cryostat by a conventional semiconducting amplifier. The wire count for multiplexing to

the base temperature stage is 8 SQ2 biases, 8 SQ2 flux biases, 8 SQ1 feedbacks lines, and 32 SQ1 row biases for a total of 56, compared to non-multiplexed readout of 256 SQUID biases and 256 SQUID feedbacks for a total of 512 signals. The total number of SQUIDs dissipating power is 8 SQ1s and 8 SQ2s for a total of 16 compared to 256 for non-multiplexed readout. Hence, multiplexing gives 9 times fewer wires and 16 times fewer biased SQUIDs.

However, there are some costs to TDM multiplexing, because the first-stage SQUID for each pixel is measuring the TES for only a fraction of the total period. The SQ1 feedback is updated at the frame rate, $t_{frame} = t_s n_{rows}$, where t_s is the period during which the multiplexer dwells on a given row, and n_{rows} is the number of rows in the column. In order to stay locked, the feedback loop needs to keep the maximum flux change in SQ1 Φ_{max} to less than approximately the flux change between the minimum and maximum of the $V-\Phi$ curve. Due to an asymmetry designed into SQ1, the maximum flux change between updates of the feedback loop is $0.65 \Phi_0$. For a simple TES, the maximum flux change¹⁶ is

$$\Delta\Phi_{max} = \rho_{max}(\Delta E) M_{in} t_{frame}, \quad (4)$$

where M_{in} is the input mutual inductance to SQ1 and $\rho_{max}(\Delta E)$ is the maximum rate of change of current for a given detector and is a function of the TES parameters and the photon energy.

$\rho_{max}(\Delta E)$ can be calculated for these devices with thermally distinct absorbers by use of the relations for TES current versus time.⁵ In the small-signal limit, $\rho_{max}(\Delta E)$ is linear in ΔE . The maximum current change in the TES occurs on the rising edge of the pulse. The slowest rising edge for a pulse of a given energy is achieved when the TES is critically damped. Usually, additional inductance is added to the TES bias circuit in order to achieve critical damping. The additional inductance is referred to as the Nyquist inductance, because it serves the dual purpose of rolling off the Johnson noise above the Nyquist frequency to prevent noise aliasing.

In TDM,¹⁷ the bandwidth of the encoded signal, set by the boxcar modulation function, is $1/(2t_s)$, while the Nyquist frequency associated with the frame rate is $1/(2t_{fr})$, so that the noise of the SQUID multiplexer is $\sqrt{n_{rows}}$ larger than a non-multiplexed signal. If we reference this to the TES current, then the current noise is

$$I_{N_SQn_{eff}} \propto \frac{\Phi_{N_SQ1}}{M_{in}} \sqrt{n_{rows}}, \quad (5)$$

where Φ_{N_SQ1} is the noise spectral density of a single first-stage SQUID.

As the number of multiplexed rows increases, it is harder to keep the SQUIDs locked in the linear range per Eq. (4), and the SQUID noise is increased per Eq. (5). Increasing M_{in} can be used to lower the effective SQUID noise, but at the cost of increasing the maximum flux change and increasing the chance of the SQUID losing lock.

In this instrument, the longest switching transient due to one SQ1 in a column being turned off and the next row turned on is measured to be 520 ns. This settling period is believed to be limited by the cryostat wiring. After switching on the SQ1 and applying the feedback calculated on the previous pass, the

multiplexer must wait for 520 ns before it begins to measure. This leaves sufficient time to average the error signal before switching again, because the shortest t_s allowed in the current multiplexing electronics is 640 ns.

The current generation of TDM multiplexer is measured to have $\Phi_{N_SQ1} = 1 \mu\Phi_0/\sqrt{Hz}$. The multiplexing chip with the best compromise of dynamic range and noise for these detectors has a $M_{in} = 278$ pH. Given these parameters, the rate of change of the current in the TES needs to be less than 0.24 A/s. The TESs are designed so that the maximum rate of change of current from a 200 keV pulse matches the 0.24 A/s limit of the multiplexed readout. The measured performance of the multiplexed readout is described in Sec. V.

Development of new multiplexing schemes will allow readout of larger arrays and faster pulses. One very promising alternative to TDM is code-division multiplexing (CDM).^{18,19} Instead of combining the signals using low-duty cycle square waves as in TDM, the signals are combined by modulating the polarity of the coupling to the SQUIDs by Walsh matrices. Since all the rows are sampled in every switching cycle, CDM does not suffer from the $\sqrt{n_{rows}}$ SQUID-noise aliasing that limits TDM. Therefore, CDM allows M_{in} to remain low at large n_{rows} , and the low M_{in} , in turn, increases the effective dynamic range for the pulses. Flux summing CDM is drop-in compatible with our existing hardware and has been demonstrated in a 1 column by 8 row configuration for the measurement of x-ray TES microcalorimeters.²⁰ Current-summed CDM, also under development, could potentially allow megapixel arrays of TESs with integrated bias and readout on the same chip as the detectors.²¹

D. Detector package and electrical interconnects

The detectors are housed inside a gold plated copper box mounted on the FAA rod at the base temperature of the cryostat. The box shields the detectors from black body radiation from the 3.5 K stage. As shown in Fig. 5(a), the detector box houses the necessary chips along with a G-10 personal computer (PC) board to route wiring to these chips. The base of the box has separate windows underneath each detector chip for access by the gamma rays. The detector box is designed to hold four detector chips, each chip separated into two bays, resulting in 256 pixels in eight bays. Besides the detector chips, each bay contains a 33 row NIST TDM chip and an interface chip, shown in Fig. 5. Each interface chip contains 32 shunt resistors and Nyquist inductors along with bonding pads to connect to both the multiplexer (MUX) chip and the detector chip. All the detectors in a bay share a detector bias that passes through the 32 shunt resistors in series. Approximately 40 gold wire bonds are used between each detector chip and the Cu box to heat sink the chip.

Figure 5(b) shows a close up view of one MUX chip and one interface chip. The MUX and interface chips are mounted on top of the PC board to simplify signal routing. The schematic overlaid on Fig. 5(b) shows how the signals are routed and the components are distributed among the detector, MUX and interface chips. The schematic shows the details of the implementation of the bias circuit from Fig. 2(a). The PC

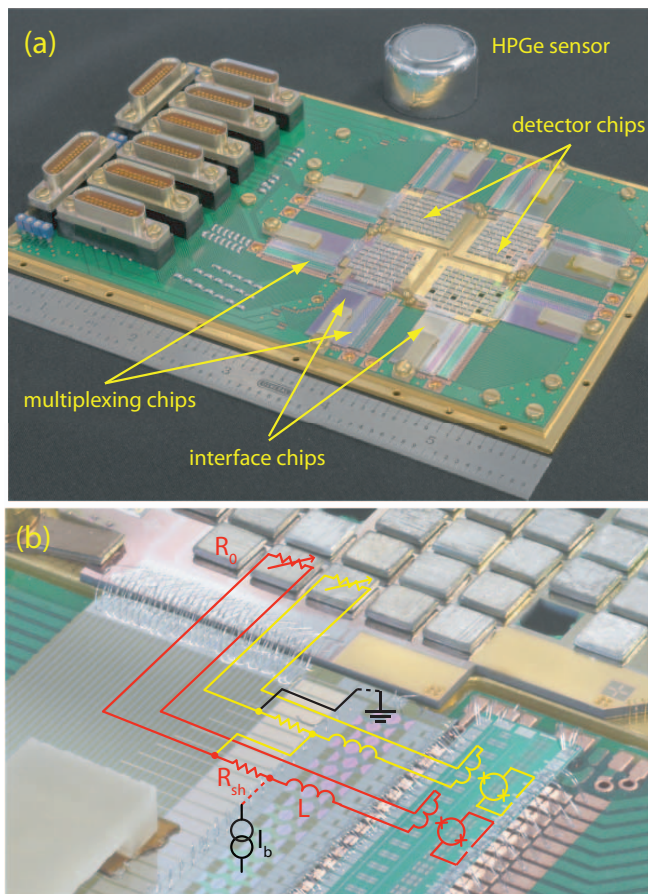


FIG. 5. (a) Photograph of the inside of a fully populated detector box showing the layout of the detector, multiplexing, and interface chips. There are two multiplexing and interface chips for each detector chip. (b) A zoomed view of the multiplexing and interface chips mounted on top of the PC board along with a schematic showing how the TES bias and readout circuits are divided among the 3 chips.

board traces moving diagonally across the photograph are the row addresses used to turn on all the SQUIDs in a given row. Since a given SQ1 bias needs to go to the corresponding row in each bay, these traces travel all the way around the box and access all eight multiplexer chips.

The shunt resistors are palladium-gold thin-films patterned as interdigitated resistors to achieve a small resistance out of higher sheet resistance material. The superconducting Nb wires also act as the lead material for the interdigitation. This makes it possible to reliably achieve small, uniform resistances without having to move to materials too thin to reliably process. The target shunt resistance (R_{sh}) for these devices is 0.3 m Ω . R_{sh} was measured for “typical” interface chips from each fabrication run using four wire measurements at 4 K and also at operating temperatures below 100 mK and was found to be within 15% of the target value at all temperatures down to the base temperature of the cryostat.

The Nyquist inductors are located on the interface chips in series with the TESs. They are fabricated from thin-film Nb in a first-order gradiometric layout. The inductance goes up approximately as the square of the number of turns. A 55-turn loop results in $L = 1.7 \mu\text{H}$, which is the predicted inductance to achieve critical damping of the TESs using two-body mi-

crocalorimeter models. A 45-turn loop, with $L = 1.2 \mu\text{H}$, is used as a fallback inductor in cases of outlier TESs. The number of turns of the inductor, 55, 45, or no turns, can be selected by the choice of wire-bonding pads. The option for no added inductance, residual $L = 20 \text{ nH}$, gives pulse rise-times that are too fast to multiplex more than a few pixels but are useful for diagnostic purposes.

The electrical connections between the base-temperature devices and the room-temperature electronics need to have low thermal conductance while maintaining low impedance and high bandwidth. Multiplexing significantly reduces the number of wires needed, but it still requires around 70 pairs of wires to read out the full array. The wiring is split into two stages, a room-temperature to 3 K stage, and a 3 K to the base-temperature stage. A PC board at 3 K provides a platform to both thermally anchor and reroute as necessary all the signal and bias lines. The package containing the 8 SQUID series-array amplifiers is also housed on this board. The PC board also allows for filtering of the lines as they pass through the flange for the 3 K radiation shield.

Ten low inductance flexible cables containing eight signal-ground pairs of CuNi conductors in microstrip geometry run between the 3 K PC board and custom electronics on the top of the cryostat. The cables are thermally anchored at the 50 K pulse-tube stage. Twisted pairs of superconducting NbTi with a CuNi coating run between 3 K and base temperature and are thermally anchored at the GGG stage.

E. Instrument efficiency

In most applications, including nuclear safeguards, high-statistics spectra are important to the success of the technique. The important role of Poisson statistics in determining peak intensities dictates that microcalorimeters must collect similar numbers of counts as HPGe within similar counting times. This implies goals for both efficiency and maximum count-rate similar to those achieved by HPGe.

Typical HPGe detectors have a maximum throughput around 40×10^3 counts per second for pulse shaping times near 2 μs . If pulse shaping times are further reduced, then the resolution begins to degrade. For our current gamma-ray microcalorimeters, we observe degraded resolution above 10 counts per second. This sets the maximum throughput for a 256-pixel array to 2.5×10^3 counts per second. Section VII discusses work in progress that will shorten the pulse time constants, allowing each pixel to operate 10 times faster, resulting in a 25×10^3 counts per second maximum throughput.

The detector array is mounted inside a copper box mounted at the base temperature of the cryostat inside a number of magnetic and radiation shields, along with the vacuum jacket. The photons from a source must pass from outside the cryostat to the detector array without being absorbed or scattered by intervening material. In the current setup, a source can be placed as close as 28 mm from the detector array. Simulations of the array package and detectors were performed using the software package GEANT4²² and these simulations were used to optimize the instrument efficiency. There are access ports cut into the 60 K, 3 K, and 50 mK shields that are covered with a 0.1 mm thick layer of aluminum tape. Other

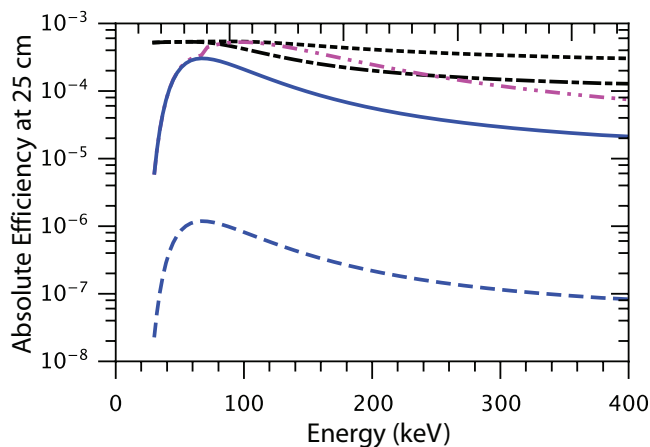


FIG. 6. Estimated absolute efficiency for a single 0.38 mm thick Sn pixel (blue dashed line), a 256 pixel array (blue solid line), and a 256 pixel array of Ta absorbers (magenta dashed-dotted-dotted line). All microcalorimeter pixels are $1.5 \text{ mm} \times 1.5 \text{ mm}$. Also shown for comparison are representative 2.5 cm diameter HPGe detectors that are 0.5 cm (black dashed-dotted line) and 1.5 cm (black dotted line) thick.

than these thin layers of aluminum, the only relevant materials in the photon path are the high-permeability magnetic shielding, which is thinned to 1 mm, and the cryostat vacuum shell, which is thinned to 2 mm of Al. Below 150 keV, the attenuation is dominated by the high-permeability magnetic shield. When important gamma-ray lines are between 20 keV and 80 keV, a hole can be cut into this shield, but this increases the probability of trapping magnetic flux in the microcalorimeters and SQUID readout. Also, for this energy range, the aluminum cryostat port can be replaced with an 0.8 mm thick carbon fiber window.

Figure 6 shows the estimated efficiency for a number of different configurations assuming a point source 25 cm from the detector. The efficiency estimates are based solely on the linear attenuation coefficients of the various materials and do not include Compton scattering or the tin escape x-rays.²² The blue dashed line shows the efficiency of a single $1.5 \times 1.5 \times 0.38 \text{ mm}$ Sn pixel. At 25 cm from a single pixel, the geometric fraction of photons incident on a single absorber is 2.9×10^{-6} . The relative efficiency of the Sn absorber is 0.37 at 100 keV. The absolute efficiency includes the attenuation from the three layers of Al tape (3% at 100 keV), the intact high-permeability magnetic shield (18% at 100 keV), and the carbon fiber window (3% at 100 keV). The solid blue line shows the absolute efficiency of the current instrument, a 256-pixel array. For a point source at 25 cm, the scaling with pixel number is close to linear. For comparison, the predicted efficiency for a planar HPGe detector that is 2.5 cm diameter by 0.5 cm thick is shown as a black dashed-dotted line, and 2.5 cm diameter by 1.5 cm thick is shown as a black dotted line.

The increase in efficiency from moving to a 256 pixel array is substantial, but to eventually achieve efficiencies better than HPGe, we need to move to much larger arrays or switch to higher Z materials while maintaining similar heat capacities. The magenta dashed-dotted-dotted line is the predicted efficiency for a similar-size piece of tantalum. However, tantalum is known to have an anomalously long pulse tail of hun-

dreds of milliseconds²³ that reduces the maximum count rate. We continue to search for higher Z materials with suitable energy resolution and speed.

F. Pulse processing and energy calibration

Once the raw pulses from the TES have been recorded, additional processing is required to produce a spectrum that can be used to determine isotopic ratios. First, pulses that have various pathologies (e.g., pulse pile-up) must be removed from the data set. Then the data are optimally filtered using knowledge about the power spectral density of the noise and an average pulse.²⁴ If there is an evidence of drift in the peak energies as a function of time, a drift correction is performed.

Finally, an energy calibration is performed using known energies in the sample or a calibration source. The output of the pulse processing is a spectrum for a single microcalorimeter. The calibrated spectra of all the pixels are co-added to form a single high-statistics spectrum.

V. CHARACTERIZATION

As described in Sec. III, the optimization of these microcalorimeters for photons in the 20 keV to 220 keV range drives choices of device parameters such as C_1 , C_2 , G_1 , G_2 , and α . If a pixel does not achieve the target parameters, its performance can suffer and it may need to be excluded from the co-added spectra. To keep the wire count low, all the microcalorimeters in a column (32) share a common detector bias. Instead of optimizing the bias for each individual detector, a bias is chosen that is a compromise of the best value for all the detectors in the column. A microcalorimeter that has significantly different parameters from the others will have degraded performance at the optimum bias points for the other detectors. Hence, array uniformity is an important factor. The importance of array uniformity helps drive the need for characterization of all 256 pixels, but the large number of microcalorimeters makes full pixel characterization difficult without automation of the measurements and data analysis.

There are 33 microcalorimeters per bay and 2 bays on each of the detector chips, for a total of 264 sensors. However, each interface chip has only 32 channels, resulting in 256 possible measurable detectors. Three of the detectors were inoperable due to problems in the readout. Finally, 17 of the pixels did not respond to the bias, so that 92% of the total 256 potential pixels had a measurable IV characteristic.

Four chips contain the 8 bays as indicated in Fig. 7. Each fabricated wafer contains four chips. Three of the chips are from one wafer, while the fourth (with Bays D and E) was from a second wafer fabricated at a later time. The position and orientation of the chips on the wafers gives insight to variations or trends across a wafer. The arrows on each chip in Figs. 7, 8, and 11 point to the top of the wafer prior to the chips being separated. The labels in the figures indicate the wafer position; top-right (TR), top-left (TL), bottom-right (BR), and bottom-left (BL).

An important parameter for both energy resolution and bias uniformity is the T_c of the individual microcalorimeters.

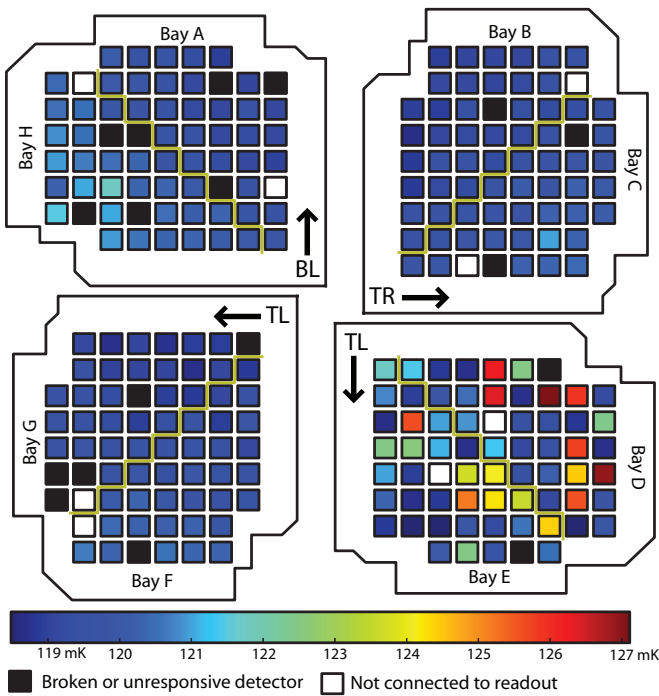


FIG. 7. Map of temperatures corresponding to 50% R_n for all pixels. The labels on each chip indicate their position from the fabricated wafer; top-right (TR), top-left (TL), and bottom-left (BL). The arrows point to the top of the wafer prior to release of the chips.

The T_c of the Mo-Cu bilayers is affected by the thickness of the layers, their deposition and processing conditions, and the copper bars and banks that are used to shape the transition. Any variation of these parameters from device to device or across a wafer will cause a variation in T_c . To measure the T_c 's on an array scale, we apply a small sinusoidal signal to the detector bias and monitor the amplitude of TES current

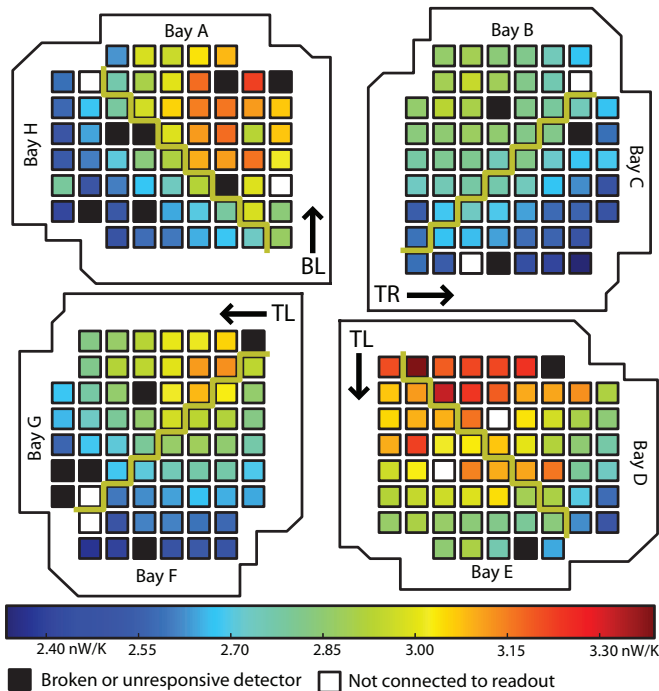


FIG. 8. Map of measured G_1 scaled to 120 mK for intercomparison.

response as a function of temperature. We define T_c as the temperature where the TES resistance is 50% R_n .

The T_c of each pixel for the full array is shown in Fig. 7. The pixels that were not wired up to the readout are shown in white and the unresponsive or broken pixels are shown in black. The mean T_c for all the pixels is 120.1 mK with a standard deviation of 1.5 mK. However, due to the common bias, the standard deviation of T_c within a bay is more relevant. The chip corresponding to bays D and E has a much higher standard deviation, 2.9 mK and 2.2 mK, respectively, while the other bays have an average standard deviation of 0.35 mK.

The equilibrium temperature (T_0) and current (I_0) for each TES at a given bias voltage (V) are determined by power balance between the Joule power and heat transfer through the membrane, resulting in

$$I_0 V = \dot{Q} = k (T_{TES}^n - T_{bath}^n). \quad (6)$$

For any two TESs, the ratio of the bias voltages to achieve the same bias point in terms of % R_n is

$$\frac{V_1}{V_2} = \left(\frac{T_{T_0:1}^n - T_{bath}^n}{T_{T_0:2}^n - T_{bath}^n} \right)^{1/2}, \quad (7)$$

assuming n and k are the same between the two devices. Assuming $T_c - T_0 \ll T_{bath}$, we can estimate the spread in voltage biases to achieve the same % R_n . For our devices, $n \approx 3$ and a typical bath temperature is 80 mK. Therefore, a ± 0.35 mK spread in T_c corresponds to around 1.2% relative spread in bias points, while the 2.9 mK standard deviation in Bay D would give a 10% relative spread.

The thermal conductance of the TES to the bath (G_1) is important in terms of energy resolution and the overall electrothermal stability of the TESs. G_1 is defined as the derivative of the heat transfer with respect to temperature,

$$G_1 = nkT_0^{n-1}. \quad (8)$$

A standard technique to estimate G_1 is to measure the IV of a device at different bath temperatures and assume power balance within the TES, $\dot{Q} = I_{TES} V_{TES}$. Equations (6) and (8) can then be used to fit for n and k along lines of constant resistance. However, I_{TES} is also a function of temperature, giving rise to a non-zero β_I . High in the transition, when the current is low and $\beta_I \approx 0$, the fits to measured $I_{TES} V_{TES}$ should be valid. Then, T_0 can be calculated from the measured power and the fit values for n and k , and then G_1 can be calculated using Eq. (8).

Figure 8 shows a map of the measured G_1 across the entire array. Each measured G_1 has been scaled by $(0.120/T_c)^{n-1}$ to compensate for differences in T_c . The mean G_1 for the entire array is 2.83 nW/K with a standard deviation of 0.2 nW/K. A $\pm \sigma$ spread in G_1 would give an approximately 7% relative spread in bias voltages to achieve the same bias point, assuming identical T_{TES} and n . Except for the T_c outliers in Bays D and E, the variation in G_1 causes most of the inhomogeneity in bias points within a bay.

If the chips are rearranged to their orientation and position on the wafers, there is a noticeable radial trend: G_1 is higher in the middle of the wafer, 3.3 nW/K, and lower on the edges of the wafer, 2.4 nW/K. This could be caused by radial

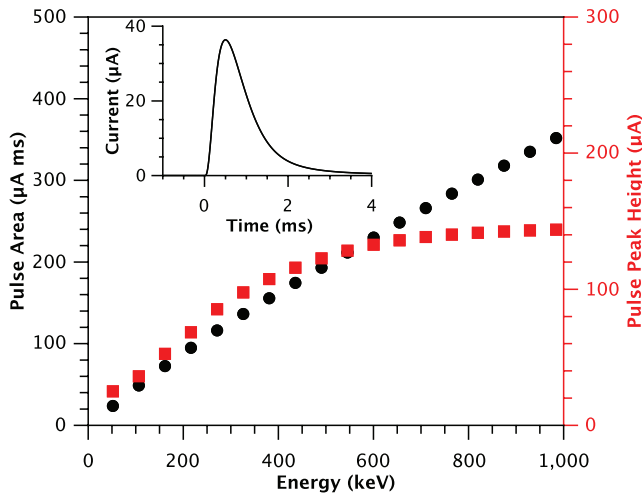


FIG. 9. The average pulse area (black circles, left axis) and peak height (red squares, right axis) as a function of pulse energy from the diode laser for one of the microcalorimeters measured at a $T_{\text{bath}} = 85$ mK and biased at 20% R_n . The inset shows TES current as a function of time in response to a 103 keV gamma ray for one of the TESs from the 256 pixel array.

non-uniformity in the etch process that removes the Si from behind the membrane. In order to fully etch the membranes in the center of the wafer where the etch rate is the lowest, we must over-etch the membranes near the perimeter. This over-etching results in larger membranes near the edge of the wafer that could explain the lower values of G_1 . A similar trend, not shown, is observed in the T_c if we ignore the high T_c outliers in bays D and E. The middle of the wafers has lower T_c and the outside has a higher T_c . Since the wafer rotates during deposition of the Mo, a slight misalignment could cause thinner Mo in the center of the wafer, resulting in lower values of T_c .

Of the 236 pixels that showed suitable superconducting transitions, all were stable at $T_{\text{bath}} = 85$ mK and 20% R_n . A typical pulse from the 103 keV gamma-ray line of a ^{153}Gd calibration source is shown in the inset of Fig. 9 for one of the microcalorimeters in this array. The 10% to 90% rise time of the pulse is measured to be 260 μs , while the 90% to 10% decay time is 1.40 ms. The maximum rate of change of the TES current for this pulse is 0.137 A/s.

Another important metric for the detectors is the dynamic range. The detectors have been designed to extend at least up to the 208 keV region, where there are useful peaks for the determination of the isotopic ratios of Pu. At these energies, the efficiency is reduced, see Fig. 6, but the gamma-rays do not saturate the TES. In order to characterize the dynamic range and linearity, we mimic gamma-rays using bursts of 1550 nm photons from a pulse-modulated diode laser. The laser allows a programmable effective pulse energy without all the sources it would take to span the full range of these detectors. For a given laser bias current, the length of the bias pulse determines the number of photons that are absorbed by each detector. Because the period, the laser is on, is small compared to the response of the TES, these bunches of photons mimic much higher energy gamma-rays. The energy response of the TES to the laser can be calibrated against a ^{153}Gd gamma-ray calibration source.

Using the laser, we can map the nonlinearity and evaluate the dynamic range of the pixels. The laser is pulsed thousands

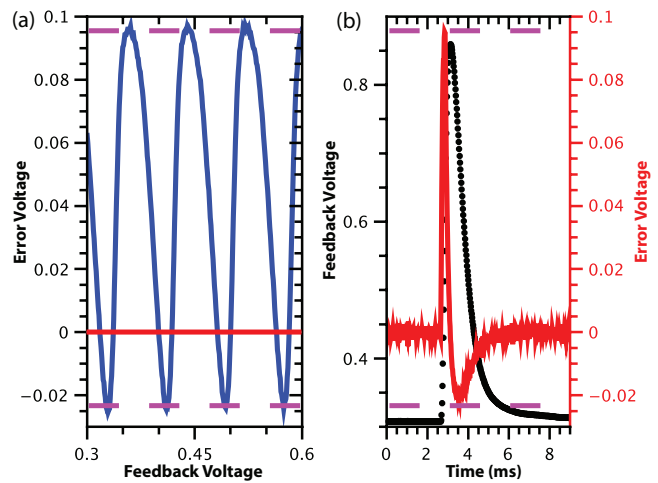


FIG. 10. (a) The measured open-loop voltage response (blue solid line) for one of the 256 SQ1s amplified by SQ2 and the series array. The dashed purple lines show the extent of the usable V- Φ range. (b) The measured closed-loop feedback (black circles (left axis)) and error signal (red solid line (right axis)) for a 215 keV pulse. For these parameters, this is the largest pulse the flux-lock loop can handle since the error signal fills the usable error range.

of times at a given pulse length, and the average current pulse height and pulse area are obtained as a function of laser pulse energy. Figure 9 shows the unfiltered pulse height and pulse area as a function of pulse energy for a single microcalorimeter. Above 400 keV, this detector begins to saturate, and the pulse height is no longer strongly correlated to energy. Information about higher energy pulses can still be obtained from the pulse area, but at a cost of degraded resolution.

The dynamic range of the individual sensors extends well past the design goal of 215 keV. However, we must achieve this dynamic range with the fully multiplexed 256-pixel array. The V- Φ curve for one of the 256 SQ1s measured through the amplifier chain is shown in Fig. 10(a), measured in an 8×32 configuration with 1.2 k Ω feedback resistor. Figure 10(b) shows the feedback voltage (black points) during the arrival of a pulse that is equivalent to 215 keV, along with the error signal (red line) created by the same pulse. The proportional and integral terms of the feedback loop are increased to the upper practical limit, where the oscillations caused by the feedback can no longer be subtracted out. In this configuration, 215 keV produces the largest error signal possible without slipping a flux quantum, since the error signal fills the whole range of the V- Φ curve; see Fig. 10(b). If we wish to measure larger pulses, we can either reduce the number of rows being multiplexed, or change the TES bias conditions to lower the maximum rate of change of the TES current. Since the maximum rate of change is approximately linear with pulse height, reducing the number of rows to 16 would increase the maximum measurable pulse energy to 425 keV. Similarly, in an eight-row configuration, the SQUIDs can maintain lock well past the energy where the detectors are saturated.

VI. INSTRUMENT PERFORMANCE

Any single microcalorimeter is not able to achieve the necessary statistics for complicated spectra that are common

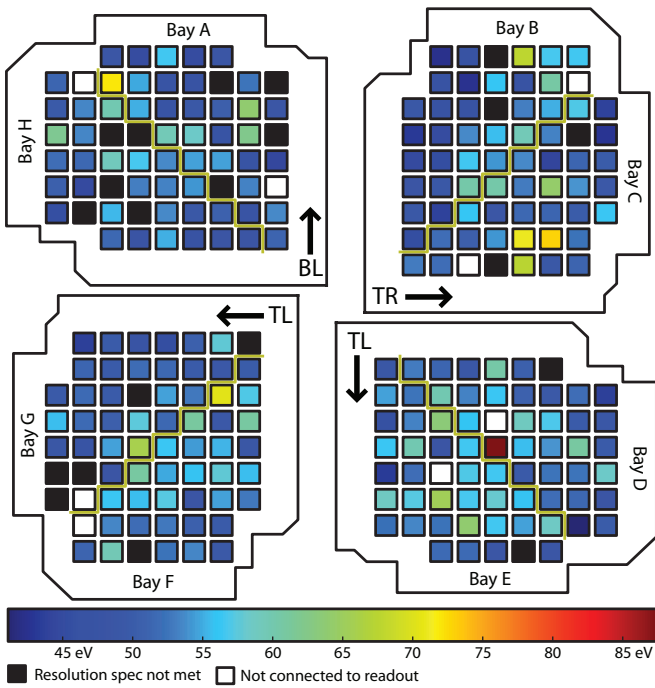


FIG. 11. Map of measured FWHM energy resolution of the 97.4 keV line of ^{153}Gd .

for our target non-proliferation samples. The spectra of all the individual microcalorimeters are co-added to produce a combined spectrum with the necessary statistics. Microcalorimeters that have significantly degraded energy resolution cannot be included in the co-added spectra because they would degrade the overall resolution and line shape. The goal of this spectrometer is to collect high-statistics spectra with better than 100 eV energy resolution in the energy regions relevant for Pu isotopic analysis. In order to achieve this goal, we need to have a large fraction of the pixels achieve better than 100 eV resolution. Figure 11 shows the measured FWHM energy resolution of the full array using the 97.4 keV gamma ray line from ^{153}Gd . These measurements were performed at a bath temperature of 85 mK and a detector bias of 20% R_n . The plot shows that 92% of the pixels have an energy resolution lower than the target resolution of 100 eV, and 90% were better than 68 eV.

Figure 12 shows a histogram of the measured FWHM energy resolutions. The average energy resolution of the 236 working pixels is 53.3 eV with a standard deviation of 6.9 eV. This compares reasonably with the predicted energy resolution from the design parameters.

Finally, Fig. 13 shows the measured spectrum of a ^{153}Gd source obtained by summing the energy-calibrated spectra of 233 of the possible 256 microcalorimeters. The microcalorimeters were multiplexed in the full 8×32 configuration, demonstrating the largest multiplexed array of TES microcalorimeters to date. The detectors were biased at an average bias point of 30% R_n and $T_{\text{bath}} = 85$ mK. This spectrum was acquired in 68 min with a median count rate of 1.41 counts per second per pixel before rejection of records with pulse pileup and a median count rate of 1.31 counts per second per pixel after rejection of records with pulse pileup.

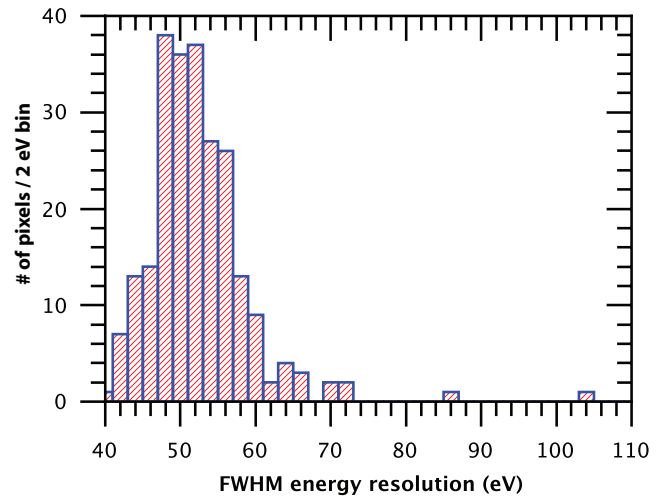


FIG. 12. A histogram of the measured energy resolutions for the 236 working pixels. The energy resolution was measured at $T_b = 85$ mK and biased at 20% of R_n .

The count rate for the entire array was 335 counts per second before rejection of records with pulse pileup and 308 counts per second after rejection of records with pulse pileup. The median unlock rate per channel was 4 mHz, mostly caused by pulses greater than 220 keV from environmental radiation and cosmic rays. Computer software that runs in parallel to the pulse acquisition software monitors the data stream and relocks a SQUID if the baseline has slipped a flux quantum.

The average resolution of the detectors (65 eV) is worse for the fully multiplexed array (8 columns and 32 rows), than when the detectors were measured in smaller batches of 8 to 16 detectors. We are currently investigating the cause of the slightly decreased energy resolution. One possibility is that between 16 and 32 rows, we reach a point where the increased SQUID noise from multiplexing more pixels begins to degrade the energy resolution. Another possibility is the detectors are less sensitive at 30% R_n than at 20% R_n , where they were measured for Figs. 11 and 12. The bias was increased to 30% R_n for the fully multiplexed measurements in order to decrease the unlock rate.

The most prominent gamma ray lines from the ^{153}Gd source are indicated by the red arrows. Also shown in the spectra are the Eu K_α complex between 40 and 42 keV and the Eu K_β complex between 46 and 49 keV. A number of the peaks in the spectra are Sn x-ray escape peaks, generated when the x-ray released by a photo-excited Sn atom escapes the sensor. The escape peaks will occur at the gamma-ray energy minus the Sn x-ray energies. The most probable x-ray energies for Sn are 25.27, 25.04, 28.49, 28.44, 29.11 keV, corresponding to the $K_{\alpha 1}$, $K_{\alpha 2}$, $K_{\beta 1}$, $K_{\beta 3}$, and $K_{\beta 2}$ lines.²² The remaining distinguishable lines are from fluorescence of the gold plating of the detector package and the lead housing of the source holder. The log scale in Fig. 13 shows that the backgrounds are different on different sides of the main photo-peaks, i.e., a few counts per bin above 103.2 keV and around 40 counts per bin below 103.2 keV.

Figures 14(a) and 14(b) show more detailed views of the 97 keV and 103 keV peaks at 2 eV bin width. The black solid lines are the measured histograms, while the red dashed lines

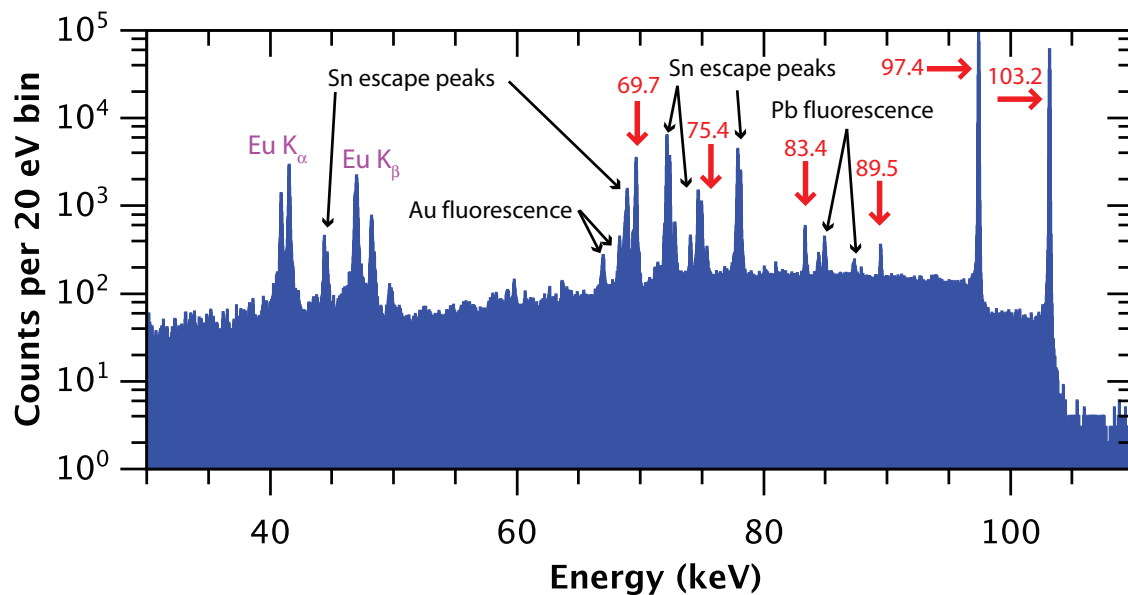


FIG. 13. Combined spectra from 233 microcalorimeters for a ^{153}Gd radioisotope source. The red arrows show the six most prominent gamma-ray lines in the spectra.

are Gaussian fits to the data, assuming a constant background. The fits give a FWHM energy resolution of 65.2 eV and 65.9 eV for the 97 keV and 103 keV peaks, respectively. The Gaussian fit misses the very tops of the photo-peaks, because the peaks are slightly non-Gaussian, due to the summing of detectors with a range of energy resolutions. Understanding how to deal with these shapes will be important for fitting data from more complex spectra. Alternatively, spectra from the individual detectors may need to be analyzed individually.

The spectra shown in Figs. 13 and 14 are a good demonstration that this instrument can achieve both high statistics and high energy resolution. Both qualities are needed to perform precise and accurate isotopic analysis. The next step for these detectors is to demonstrate similar performance while measuring more complicated spectra, such as mixed isotopes of Pu or samples relevant for spent fuel reprocessing.

VII. FUTURE WORK

The current instrument achieves the design goals; it has better than 100 eV resolution at 100 keV with efficiencies that

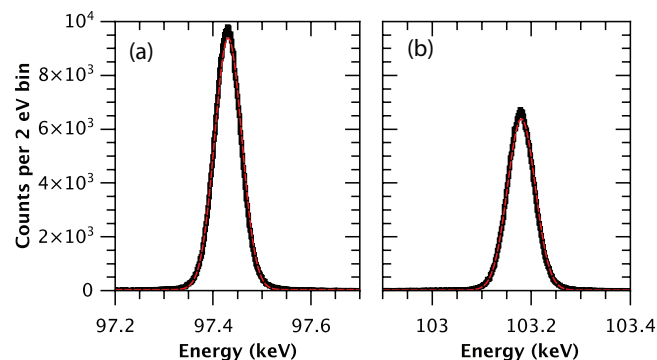


FIG. 14. (a) and (b) are the combined spectra for the 97.4 and 103.2 keV peaks (black solid lines) along with Gaussian fits (red dashed lines) giving a FWHM resolution for the combined spectra of 65.2 eV and 65.9 eV.

approach what is achieved by state-of-the-art HPGe detectors. As described in Sec. IV C, new multiplexing schemes should enable larger arrays, even to megapixel scales, that achieve still higher efficiency. However, there are a number of other areas where the instrument can be improved in the short term.

We have measured that our achieved energy resolution in previous arrays worsened as the count rate increased above a few Hertz. The degradation of the energy resolution is caused by thermal and electrical cross-talk between pixels. Small amounts of cross talk can quickly degrade energy resolution when attempting spectroscopy at a part in 1000 resolving power. We are in the process of characterizing the crosstalk and will use this information to redesign the sample box and the layout of the interface and readout chips.

We have also observed that the measured pulses from the microcalorimeters have an additional longer time constant during their decay.¹¹ This additional time constant is usually a factor of ten longer than the thermal time constant expected from detector models and, as a result, is usually referred to as the athermal tail. There are a number of possible explanations for the athermal tail, including the amorphous glue used to attach the absorber¹¹ and a quasiparticle bottleneck in the Sn absorber.²⁵ Understanding the origin of this athermal tail and mitigating its effects could reduce pulse pileup. Eliminating the athermal tail, combined with improvements in the cross-talk would allow for more than an order-of-magnitude improvement in count rate. Work on new pulse processing algorithms, including running-sum algorithms and alternate optimal filters that are more robust to pulse pileup, will eventually allow even higher count rates.²⁶

We are also pursuing alternative absorber materials that could be used to make higher efficiency absorbers with the same or reduced heat capacity. Attempts to use some potential replacements, i.e., tantalum, have been frustrated by extremely long athermal time constants. Tantalum shows an athermal time constant that is ten to a hundred times longer

than that of tin.²³ The search for alternate absorber materials continues to be an area of active research.^{27,28}

VIII. CONCLUSION

The NIST-LANL gamma-ray spectrometer has demonstrated an average FWHM energy resolution of 53 eV at 97 keV, with a useable dynamic range above 400 keV. The array of TES microcalorimeters has a collecting area of 5 cm² and efficiencies similar to that of HPGe. This collecting area is achieved by multiplexing a 256-pixel array in a 8-column by 32-row configuration. In this paper, we have presented the design and fabrication of the detectors and instrument that make this combination of resolution and efficiency possible. We are in the process of measurements to demonstrate similar resolution and yield while measuring more complicated spectra from materials relevant to the nuclear fuel cycle.

This instrument will be a valuable tool to assess the impact of microcalorimeters on nuclear materials accounting and nuclear safeguards. The instrument can also have impact on other applications that require ultra-high-resolution gamma-ray and hard x-ray spectroscopy. These applications include the determination of gamma- and x-ray line positions with metrological accuracy, gamma-ray astrophysics, spectroscopy of terrestrial plasmas at electron beam ion traps and other unusual facilities, and Fermi surface mapping through Compton scattering. Considering only the last example for brevity, the use of energy-dispersive microcalorimeters for Compton scattering experiments promises dramatic improvements in momentum resolution and collecting efficiency over the detection techniques presently used. When combined with the traditional attractions of Compton scattering, namely bulk sensitivity and relaxed surface preparation requirements, the improvements provided by microcalorimeter detectors may allow Fermi surface measurements on much broader classes of material than are presently possible.

ACKNOWLEDGMENTS

We gratefully acknowledge the support of the U.S. Department of Energy through the Office of Nonproliferation Research and Development.

¹M. K. Bacrania, A. S. Hoover, P. J. Karpus, M. W. Rabin, C. R. Rudy, D. T. Vo, J. A. Beall, D. A. Bennett, W. B. Doriese, G. C. Hilton, R. D. Horansky, K. D. Irwin, N. Jethava, E. Sassi, J. N. Ullom, and L. R. Vale, *IEEE Trans. Appl. Supercond.* **56**, 2299 (2009).

²M. Rabin, *AIP Conf. Proc.* **1185**, 725 (2009).

³K. Irwin and G. Hilton, *Cryogenic Particle Detection*, Topics in Applied Physics, Vol. 99 (Springer-Verlag, 2005), pp. 63–149.

⁴A. S. Hoover, M. K. Bacrania, N. J. Hoteling, P. J. Karpus, M. W. Rabin, C. R. Rudy, D. T. Vo, J. A. Beall, D. A. Bennett, W. B. Doriese, G. C.

Hilton, R. D. Horansky, K. D. Irwin, J. N. Ullom, and L. R. Vale, *J. Radioanal. Nucl. Chem.* **282**, 227 (2009).

⁵D. A. Bennett, R. D. Horansky, A. S. Hoover, N. J. Hoteling, M. W. Rabin, D. R. Schmidt, D. S. Swetz, L. R. Vale, and J. N. Ullom, *Appl. Phys. Lett.* **97**, 102504 (2010).

⁶J. Ullom, J. Beall, W. Doriese, W. Duncan, L. Ferreira, G. Hilton, K. Irwin, C. Reintsema, and L. Vale, *Appl. Phys. Lett.* **87**, 194103 (2005).

⁷W. B. Doriese, J. N. Ullom, J. A. Beall, W. D. Duncan, L. Ferreira, G. C. Hilton, R. D. Horansky, K. D. Irwin, J. A. B. Mates, C. D. Reintsema, L. R. Vale, Y. Xu, B. L. Zink, M. W. Rabin, A. S. Hoover, C. R. Rudy, and D. T. Vo, *Appl. Phys. Lett.* **90**, 193508 (2007).

⁸W. Holland, W. Duncan, B. Kelly, K. Irwin, A. Walton, P. Ade, and E. Robson, *Proc. SPIE*, **4855**, 1–18 (2003).

⁹J. Ullom, W. Doriese, G. Hilton, J. Beall, S. Deiker, W. Duncan, L. Ferreira, K. Irwin, C. Reintsema, and L. Vale, *Appl. Phys. Lett.* **84**, 4206 (2004).

¹⁰A. S. Hoover, N. Hoteling, M. W. Rabin, J. N. Ullom, D. A. Bennett, P. J. Karpus, D. T. Vo, W. B. Doriese, G. C. Hilton, R. D. Horansky, K. D. Irwin, V. Kotsubo, D. W. Lee, and L. R. Vale, *Nucl. Instrum. Methods Phys. Res. A* **652**, 302 (2011).

¹¹R. Horansky, J. Beall, K. Irwin, and J. Ullom, *AIP Conf. Proc.* **1185**, 733–736 (2009).

¹²V. Pecharsky and K. Gschneidner, *J. Magn. Magn. Mater.* **200**, 44 (1999).

¹³J. Ullom, W. Doriese, G. Hilton, J. Beall, S. Deiker, K. Irwin, C. Reintsema, L. Vale, and Y. Xu, *Nucl. Instrum. Methods Phys. Res. A* **520**, 333 (2004).

¹⁴C. Reintsema, J. Beyer, S. Nam, S. Deiker, G. Hilton, K. Irwin, J. Martinis, J. Ullom, L. Vale, and M. Macintosh, *Rev. Sci. Instrum.* **74**, 4500 (2003).

¹⁵M. Huber, P. Neil, R. Benson, D. Burns, A. Corey, C. Flynn, Y. Kitaygorodskaya, O. Massihzadeh, J. Martinis, and G. Hilton, *IEEE Trans. Appl. Supercond.* **11**, 4048 (2001).

¹⁶W. Doriese, J. Beall, W. Duncan, L. Ferreira, G. Hilton, K. Irwin, C. Reintsema, J. Ullom, L. Vale, and Y. Xu, *Nucl. Instrum. Methods Phys. Res. A* **559**, 808 (2006).

¹⁷K. Irwin, *Physica C* **368**, 203 (2002).

¹⁸M. D. Niemack, J. Beyer, H. M. Cho, W. B. Doriese, G. C. Hilton, K. D. Irwin, C. D. Reintsema, D. R. Schmidt, J. N. Ullom, and L. R. Vale, *Appl. Phys. Lett.* **96**, 163509 (2010).

¹⁹K. D. Irwin, M. D. Niemack, J. Beyer, H. M. Cho, W. B. Doriese, G. C. Hilton, C. D. Reintsema, D. R. Schmidt, J. N. Ullom, and L. R. Vale, *Supercond. Sci. Technol.* **23**, 034004 (2010).

²⁰G. M. Stiehl, W. B. Doriese, J. W. Fowler, G. C. Hilton, K. D. Irwin, C. D. Reintsema, D. R. Schmidt, D. S. Swetz, J. N. Ullom, and L. R. Vale, *Appl. Phys. Lett.* **100**, 072601 (2012).

²¹K. Irwin, H. Cho, W. Doriese, J. Fowler, G. Hilton, M. Niemack, C. Reintsema, D. Schmidt, J. Ullom, and L. Vale, *J. Low Temp. Phys.* **167**, 1 (2012).

²²A. S. Hoover, M. K. Bacrania, P. J. Karpus, M. W. Rabin, C. R. Rudy, D. T. Vo, J. A. Beall, W. B. Doriese, G. C. Hilton, R. D. Horansky, K. D. Irwin, J. N. Ullom, and L. R. Vale, *IEEE Trans. Appl. Supercond.* **56**, 2294 (2009).

²³R. D. Horansky, J. N. Ullom, J. A. Beall, W. B. Doriese, W. D. Durican, L. Ferreira, G. C. Hilton, K. D. Irwin, C. D. Reintsema, L. R. Vale, B. L. Zink, A. Hoover, C. R. Rudy, D. M. Tournear, D. T. Vo, and M. W. Rabin, *Nucl. Instrum. Methods Phys. Res. A* **579**, 169 (2007).

²⁴A. Szymkowiak, R. Kelley, S. Moseley, and C. Stahle, *J. Low Temp. Phys.* **93**, 281 (1993).

²⁵E. Perinati, M. Barbera, A. Collura, S. Serio, and E. Silver, *Nucl. Instrum. Methods Phys. Res. A* **531**, 459 (2004).

²⁶B. K. Alpert, W. B. Doriese, J. W. Fowler, and J. N. Ullom, *J. Low Temp. Phys.* **167**, 582 (2012).

²⁷E. Perinati, M. Barbera, S. Varisco, E. Silver, J. Beeman, and C. Pigot, *Rev. Sci. Instrum.* **79**, 053905 (2008).

²⁸P. Dreiske, M. Carmody, C. H. Grein, J. Zhao, R. Bommena, C. A. Kilbourne, R. Kelley, D. McCammon, and D. Brandl, *J. Electron. Mater.* **39**, 1087 (2010).